Revision 2

Tetrahedral boron in natural and synthetic HP/UHP tourmaline: Evidence from Raman spectroscopy, EMPA, and single crystal XRD

Authors:

Martin Kutzschbach[1,2,*], Bernd Wunder[1], Dieter Rhede[1], Monika Koch-Müller[1], Andreas Ertl[3,4], Gerald Giester[4], Wilhelm Heinrich[1], Gerhard Franz[2]

[1]GeoForschungsZentrum Potsdam, 14473 Potsdam, Germany

[2]Fachgebiet Mineralogie-Petrologie, Technische Universität Berlin, 13355 Berlin, Germany

[3] Mineralogisch-Petrographische Abt., Naturhistorisches Museum, 1010 Vienna, Austria

[4]Department of Mineralogy and Crystallography, University of Vienna, 1090 Vienna, Austria

*E-mail: mkutz@gfz-potsdam.de

ABSTRACT

Olenitic tourmaline with high amounts of tetrahedral B (up to 2.53 $^{[4]}$B pfu) has been synthesized in a piston-cylinder press at 4.0 GPa, 700 °C and a run duration of 9 days. Crystals are large enough (up to 30 x 150 μm) to allow for reliable and spatially resolved quantification of B by electron microprobe analysis (EMPA), single-crystal X-ray diffraction, and polarized single-crystal Raman spectroscopy. Tourmalines with radial acicular habit are zoned in $^{[4]}$B-concentration (core: 2.53(25) $^{[4]}$B pfu; rim: 1.43(15) $^{[4]}$B pfu) whereas columnar crystals are chemically homogeneous (1.18(15) $^{[4]}$B pfu). An amount of 1.4(1) $^{[4]}$ B pfu was found in the columnar tourmaline by single-crystal structure refinement (SREF) (R = 1.94%). The EMPA identify $^{[T]}Si_{-1}{}^{[V,W]}O_{-1}{}^{[T]}B_1{}^{[V,W]}(OH)_1$ as the main and $^{[X]}\square_{-1}{}^{[T]}Si_{-1}{}^{[X]}Na_1{}^{[T]}B_1$ as minor exchange vectors for $^{[4]}$B-incorporation, which is supported by the SREF. Due to the restricted and well-defined variations in chemistry, Raman bands in the OH-stretching region (3000 - 3800 cm^{-1}) are unambiguously assigned to a specific cation arrangement. We found the sum of the relative integrated intensity (I_{rel}) of two low frequency bands at 3284 - 3301 cm^{-1} (ν1) and 3367 – 3390 cm^{-1} (ν2) to positively correlate with the $^{[4]}$B concentrations: $^{[4]}$B [pfu] = 0.03(1) * [I_{rel} (ν1) + I_{rel} (ν2)]. Hence, those bands correspond to configurations with mixed Si/B occupancy at the T site. Our semi-quantitative correlation also holds for well-characterized natural $^{[4]}$B-bearing tourmaline from the Koralpe, Austria.

Keywords: Tourmaline, tetrahedral boron, high-pressure synthesis, single-crystal XRD, polarized Raman spectra, Koralpe tourmaline

INTRODUCTION

Tourmaline has an enormous potential for petrogenetic studies and has successfully been used as a geochemical recorder of temperature (*e.g.*, van Hinsberg and Schumacher 2007), pressure (Berryman et al. 2015b) and fluid composition (*e.g.*, von Goerne et al. 2001). Taking into account its wide stability field ranging from sub-surface (Henry et al. 1999; Moore et al. 2004) to ultrahigh-*P* conditions (Krosse 1995), and that tourmaline preserves its composition throughout its *P*-*T* history due to low element diffusivities (Henry and Dutrow 1996), tourmaline is considered with good reason *"an ideal indicator of its host environment"* (van Hinsberg et al. 2011).

The reason for the widespread occurrence of tourmaline is its flexible crystal structure, which can accommodate a large variety of site occupants. Its general formula is written as $^{[9]}X^{[6]}Y_3{}^{[6]}Z_6{}^{[4]}T_6O_{18}(^{[3]}BO_3)_3V_3W$ (Henry et al. 2011), where the most common ions (or vacancy, □) at each site are X = Na^{+}, Ca^{2+}, K^{1+}, □; Y = Fe^{2+}, Mg^{2+}, Mn^{2+}, Al^{3+}, Li^{1+}, Fe^{3+}, Cr^{3+}; Z = Al^{3+}, Fe^{3+}, Mg^{2+}, Cr^{3+}; T = Si^{4+}, Al^{3+}, B^{3+}; B = B^{3+}; V = OH^{1-}, O^{2-}; and W = OH^{1-}, F^{1-}, O^{2-}. The olenite endmember stoichometry is $NaAl_3Al_6Si_6O_{18}(BO_3)_3O_3(OH)$, a Mg-Fe free tourmaline with full occupation of the X-site and only one OH-group per formula unit (pfu).

Tourmaline is the most important carrier of B in crustal rocks and its B isotope composition extends the applicability of tourmaline to a geochemical tracer for geological mass transfer (*e.g.*, Marschall et al. 2006) and metasomatic processes (Trumbull et al. 2009; Bast et al. 2014). B isotope fractionation between tourmaline and fluid is not only *T*-dependent (Meyer et al. 2008) but also strongly affected by the structural bonding environment of B (Kowalski et al. 2013). Thus, for a thorough interpretation of B isotope data, the quantification of accurate B concentrations at the two structural positions ($^{[3]}$B and $^{[4]}$T) is essential.

In most tourmalines, B is exclusively three-fold coordinated, with three O surrounding B in a trigonal planar coordination (Clark et al. 2008). The two substitutions $^{[3]}\square \leftrightarrow {}^{[3]}B$ and 3 H $\leftrightarrow {}^{[3]}B$ leading to $^{[3]}B$ deficiency (Hawthorne 1996) are only hypothetical, as no tourmaline with less than 3 B pfu has been described so far. We thus follow Henry et al. (2011) who stated that *"the B site exclusively contains B"* and for any tourmaline composition given in this study we assume full occupation at this site, i.e. three $^{[3]}B$ pfu.

There is now general agreement that tourmaline can incorporate additional B substituting Si at the tetrahedral position. Wodara (1996) was first to synthesize olenitic tourmaline with about 2.27 $^{[4]}B$ pfu at 2.5 GPa and 600 °C and further chemical, spectroscopic and structural investigations (Schreyer et al. 2000; Marler et al. 2002) on these synthetic tourmalines confirmed their high amount of excess B. In natural tourmaline up to 1.23 $^{[4]}B$ pfu has been determined (*e.g.*, Ertl et al. 1997; 2005; 2006; 2007; Hughes et al. 2000; 2004; Kalt et al. 2001; Marschall et al. 2004; Schreyer et al. 2002; Tagg et al. 1999). $^{[4]}B$-bearing tourmaline is often described from high-*P* environments and for Al-rich stoichiometries, *i.e.*, tourmalines with a large olenitic component.

Electron microprobe analysis (EMPA) is the method routinely applied to determine concentrations of elements with $Z > 9$, whereas accurate analysis of B remains rather difficult (Bastin and Heijligers 1990). Therefore, to confidently detect $^{[4]}B$ and to determine its abundance, EMP-data need a complementary monitor. Additional methods successively applied so far comprise X-ray diffraction (Hughes et al. 2001), secondary ion mass spectrometry (Kalt et al. 2001), nuclear magnetic resonance spectroscopy (Marler and Ertl 2002; Lussier et al. 2009) and electron energy loss spectroscopy (Schreyer et al. 2000). These techniques are partially destructive and require a lot of effort with respect to sample preparation and data evaluation. In contrast, Raman scattering is far more convenient and a few studies indeed show that the

frequency of the OH-stretching vibration in tourmaline is systematically coupled to atomic number, size and charge of neighboring cations and hence, tourmaline composition (*e.g.*, Skogby et al. 2012; Fantini et al. 2014; Berryman et al. 2015a). Therefore, Raman scattering potentially provides a quantitative and easy-to-use tool to determine $^{[4]}$B contents but it needs accurate band assignments. Schreyer et al. (2000) attributed an infrared (IR) band at 3367 cm^{-1} to the occurrence of $^{[4]}$B in synthetic olenitic tourmaline using a powder of synthetic tourmaline pressed in a KBr pellet. Since then, no systematic spectroscopic study has been undertaken to evaluate the effect of $^{[4]}$B on the OH-stretching vibration of synthetic tourmaline single crystals, most likely because of the insufficient crystal size.

Here, we synthesized olenitic tourmalines large enough for polarized single-crystal investigation by Raman spectroscopy. In addition, EMP and X-ray diffraction (XRD) analysis reveal large amounts of B in excess of 3 B pfu. The results enable us to assign Raman bands related to the incorporation of $^{[4]}$B, hence, allowing for semi-quantitative determination of $^{[4]}$B contents in the synthetic tourmalines. We also apply this method to natural $^{[4]}$B-bearing tourmaline from the Koralpe, Austria.

EXPERIMENTAL AND ANALYTICAL METHODS AND SAMPLE MATERIAL

Experimental methods

To synthesize olenitic tourmaline in the system Na_2O-Al_2O_3-SiO_2-B_2O_3-H_2O, the starting material consisted of a solid homogenous mixture of quartz, γ-Al_2O_3, H_3BO_3 and a 5.4 mol/l NaCl solution. To encourage the incorporation of $^{[4]}$B, we used 300 mol% H_3BO_3 in excess to the olenite endmember stoichometry and a 5 mol%-deficiency of SiO_2, respectively. 14 mg of the solid mixture and 6 mg of fluid were loaded into a gold capsule of 13 mm in length and 3 mm in

diameter, resulting in an excess of 200 mol% NaCl relative to the olenite endmember. After loadings, the capsule was welded shut. To ensure a proper seal, the capsule was reweighed after being placed in an oven at 100 °C for a few hours.

Synthesis conditions were 4.0 GPa, 700 °C, and 9 days of duration using an endloaded piston-cylinder apparatus with a halite-pyrophyllite setup as pressure transmitting assembly. Pressure was calibrated using the quartz-coesite transition (Mirwald and Massonne 1980) with a precision of ±50 MPa. A metal furnace was used for heating and temperature was controlled with a NiCr/Ni thermocouple with a precision of ±10 °C. After pressurization, the target temperature was reached within 30 minutes. The experiment was quenched isobarically to a temperature below 200 °C in about 10 seconds. After weighing, the capsule was opened and the solid product was washed under doubly distilled water to remove any remaining boric acid or soluble quench phases. After drying, about 3 mg of the solid product was ground in an agate mortar and placed between two X-ray transparent kapton foils for powder XRD analysis. Unground solids were prepared for analysis with the scanning electron microscope (SEM) and a further portion was embedded in 1-inch round epoxy holders for EMPA. Some large tourmaline crystals were handpicked from the leftovers for single-crystal XRD structure refinement (SREF) and for polarized single-crystal Raman spectroscopy.

Tourmaline from the Koralpe, Austria

The Koralpe pegmatite is a rather small (3 – 4 m^3) intrusive body, which is exposed East of the Stoffhütte, Austria (Kalt et al. 2001). Within the main pegmatite, tourmaline occurs as an accessory phase closely adjoining plagioclase, quartz and muscovite. At the contact to the country rock it is concentrated in tourmalinite layers. Tourmaline within the pegmatite is mainly olenitic and exhibits extensive color zoning due to higher schorl and lower olenitic component in

the core compared to the rim. Its $^{[4]}$B concentrations increase from 0.35 $^{[4]}$B pfu in the core to 0.88 $^{[4]}$B pfu in the rim (EMP data in Kalt et al. 2001). Rare colorless crystals exhibit the highest B-concentration (up to 16.06 wt% B_2O_3 by EMP analysis, corresponding to 1.23 $^{[4]}$B pfu, Ertl et al. 1997) among all natural tourmalines known so far. Its T site occupancy was re-determined by Ertl et al. (2008) to $[Si_{4.89}B_{0.83}Al_{0.27}Be_{0.01}]$.

The country rock is a mylonitic garnet-mica schist metamorphosed under high *P-T* conditions (1.8 - 2.1 GPa and 580 - 650 °C) during the Eo-Alpine metamorphic overprint (100 ± 10 Ma; Miller, 1990; Strüwe and Powell, 1995; Miller and Thöni, 1997). Ertl and Brandstätter (1998) assumed that the olenite-bearing pegmatite experienced the same metamorphic event.

The natural tourmaline crystal analyzed in this study by EMP and single-crystal Raman spectroscopy was sampled from the main pegmatite body about 2 cm away from the contact with the host rock. It is dark-green in the core and light green in the rim and about 8 x 3 mm in size. Rim and core compositions of similar pegmatitic tourmalines from the same location are given in Kalt et al. (2001, their Table 1).

Analytical methods

Powder X-ray diffraction. Powder XRD analysis was performed with a STOE Stadi-P diffractometer equipped with a Cu cathode operated at 40 kV and 40 mA. A primary Ge monochromator provided convergent $CuK\alpha_1$ radiation. Diffraction patterns were recorded with a 7° wide position-sensitive detector in transmission between 5° and 125° 2θ at a step width of 0.01° 2θ. Unit-cell parameters, other structural parameters and phase proportions were refined using the GSAS software package for Rietveld refinement (Larson and Von Dreele 1987). All X-ray reflections could be attributed to olenitic tourmaline, coesite, and $AlBO_3$. For the Rietveld

refinement the initial structural data were taken from the Inorganic Structure Database (ICSD, Karlsruhe).

EMPA. The synthetic tourmaline compositions were determined with wavelength-dispersive X-ray spectroscopy (WDX) using a JEOL Hyperprobe JXA-8500F equipped with a thermal field emission gun and 5 spectrometers. To avoid disintegration of the delicate crystals we used a low beam current of 5 nA. Accelerating voltages of 10 kV, a small beam diameter of 2 μm and a careful selection of measurement spots ensured that the stimulated volume was not contaminated by phases other than tourmaline. A liquid nitrogen cold trap was used to reduce effects of hydrocarbon contamination. Natural schorl (B), jadeite (Na) and pyrope (Si, Al) were used as standards. Counting times on the peaks/background were 20/10 s for Si, 30/15 s for Na and Al, and 80/40 s for B. Background intensities were collected at higher and lower energies relative to the corresponding K_α line. Raw data were processed by applying a $\varphi(\rho Z)$ correction scheme (CITZAF; Armstrong 1995). Relative analytical errors (1σ) are: ~1% for Al, ~1.2% for Si, ~3% for Na and ~5% for B. Element maps were recorded in WDX mode using a "zero diameter" beam at an accelerating voltage of 6.0 kV and a probe current of 20 nA. In the stage-scanning mode a step size of 0.2 μm was used in X and Y directions. The counting time for each step was 2000 ms.

Compositions of natural tourmaline were obtained at similar conditions. Additional standards were orthoclase (K), hematite (Fe), rhodonite (Mn), wollastonite (Ca), periclase (Mg) and rutile (Ti) using counting times of 30 s on the peak and 15 s on the background. Kalt et al. (2001) reported that the Koralpe tourmalines contain minor amounts of Li_2O (0.47 - 0.49 wt%), F (0.09 - 0.11 wt%) and ZnO: (0.04 – 0.06 wt%), which were not analyzed in our study.

For formula calculations the EMP data was normalized to 18 cations at the Y, Z, T and B sites. For natural tourmaline we assumed total iron as Fe^{2+} and total manganese as Mn^{2+}.

Single-crystal X-ray diffraction refinement (SREF). An untwinned 60 x 25 x 25 mm large columnar single crystal showing sharp X-ray reflections was chosen for measurement with a Bruker APEXII diffractometer equipped with a CCD area detector and an Incoatec Microfocus Source IμS (30 W, multilayer mirror, Mo-K_α). A dataset up to 60° 2θ was collected at room temperature. The data were integrated and corrected for Lorentz and polarization factors with an absorption correction by evaluation of partial multiscans. The structure was refined with SHELXL97 (Sheldrick 1997) using scattering factors for neutral atoms and a starting model for tourmaline from Ertl et al. (2012). The H atom bonded to the O3 atom was located from a difference-Fourier map and subsequently refined with an isotropic displacement parameter (U_{iso}). For all non-hydrogen atoms, refinement was performed with anisotropic displacement parameters, which were used to calculate an equivalent isotropic displacement parameter (U_{eq}) (Table 3).

Polarized single-crystal Raman spectroscopy. Room temperature spectra of synthetic and Koralpe tourmaline were recorded by using a HORIBA Jobin LabRAM HR800 UV-VIS spectrometer with a grating of 1800 grooves/mm. The 488 nm line of a coherent Ar^+ laser model Innova 70-3 with a power of 145 mW was used for excitation, which corresponds to about 20 mW on the sample. The inherent polarization of the excitation laser light is coincident with the y direction of the microscope stage (N-S direction), which allowed orientation-dependent measurements with the electric field vector, E, of the light parallel and perpendicular to the crystallographic *c* axis ($E \parallel c$ and $E \perp c$) by rotating the sample. Using a 100x objective, spot sizes were 3-5 μm. Energy of the scattered photons was determined with a peltier cooled CCD detector at a resolution of about 1 cm^{-1}. Acquisition time for each spectrum was 20 s and 10 accumulations were performed for noise reduction. The region of the OH-stretching vibration was monitored between 2800 and 4000 cm^{-1}. Three spectral windows were required resulting in a

total time of 10 min per measurement. To avoid spectral contributions from the supporting medium, we placed the tourmaline crystals onto a KBr pellet. Prior to analyses the synthetic samples were heated overnight at 170 °C to remove adsorbed surface water. Blank measurements on the KBr pellet before and after the acquisition of the tourmaline spectra proved that spectral contribution of remaining surface water is below the detection limit. Raman spectra of natural Koralpe tourmaline were recorded from an epoxy-embedded crystal, which previously has been analyzed by EMP. Prior to the Raman measurements the carbon coating of the section was removed. After subtracting a linear background, the spectra were fitted with the program PeakFit by Jandel Scientific. Peak shape functions were set to Gaussians. Standard deviations (1 σ) for peak position, relative integrated intensity (I_{rel}), and full width at half maximum (FWHM) were calculated from averaging *n* individual measurements when $n > 1$. The errors for the fit of the spectrum of the acicular tourmaline core are calculated from the fit itself. The r^2 value (goodness) of each individual fit is 0.999.

RESULTS

Powder XRD and SEM

A powder XRD pattern of the experimental run product and its Rietveld refinement (Durbin Watson statistic = 1.26; $Chi^2 = 1.30$) show that tourmaline (87 wt%) formed as the most abundant phase together with coesite (12 wt%) and traces of $AlBO_3$ (1 wt%). No other phases are present. The tourmaline crystals are either idiomorphic, prismatic crystals (denoted “columnar” in the following) or form acicular, radially grown aggregates (denoted “acicular” in the following). Columnar tourmalines are up to 150 μm in length parallel to the *c*-axis and are generally 1 - 10 μm wide (Fig. 1); a few crystals up to a width of 30 μm are present. Acicular tourmalines

forming aggregates are generally smaller. Coesite appears rarely idiomorphic (Fig. 1) and mostly as fine-grained material (< 10 µm) together with minor amounts of $AlBO_3$.

The unit cell dimensions derived for the synthetic tourmaline powder are a = 15.6209(9) Å; c = 7.0307(7) Å; V = 1485.7(2) Å^3. Although tourmaline diffraction peaks are apparently symmetric, we will later show that acicular crystals exhibit significant chemical zonation. A similar small cell-volume of 1484(2) Å^3 was determined from powder diffraction of synthetic $^{[4]}$B-bearing olenitic tourmaline with 2.27 $^{[4]}$B pfu (Schreyer et al. 2000). The mean <T-O> distance is 1.590(5) Å, which is significantly smaller than the ideal <Si-O> bond length of 1.62 Å in an undistorted tetrahedron (Hawthorne 1996). Both the small cell-volume and the small mean <T-O> bond length strongly indicate substantial $^{[4]}$B-contents in the synthetic tourmaline.

EMP analyses

Synthetic tourmaline. Backscattered electron (BSE) contrast indicates that the columnar tourmalines are chemically homogenous, whereas the acicular crystals are strongly zoned (Fig. 2a). As indicated by element mapping, this zonation is due to B enrichment and Si depletion in the core compared to the rim (Fig. 2b, c). The Al content is nearly constant across the grains with apparently slightly higher Al concentration in the core (Fig. 2d). Supplementary to the SEM investigations, coesite has been detected as inclusion throughout the columnar tourmaline crystals and in the rims of the acicular grains (Fig. 2), but not in the cores. $AlBO_3$ also forms inclusions throughout the tourmaline crystals (Fig. 2).

The structural formula for columnar tourmaline is:

$^{[X]}(Na_{0.57(9)}\square_{0.43(9)})\ ^{[Y]}(Al_{3.00(0)})\ ^{[Z]}(Al_{5.92(8)}Si_{0.08(8)})\ ^{[T]}(Si_{4.82(15)}B_{1.18(15)}O_{18})$

$(BO_3)_3\ ^{[V,W]}[(OH)_{2.53(9)}O_{1.47(9)}]$.

For the acicular tourmaline the following average rim and core compositions resulted:

rim: $^{[X]}(Na_{0.66(7)}\square_{0.34(7)})\ ^{[Y]}(Al_{3.00(0)})\ ^{[Z]}(Al_{5.96(4)}Si_{0.04(4)})\ ^{[T]}(Si_{4.55(14)}B_{1.43(15)}Al_{0.02(3)}O_{18})$ $(BO_3)_3\ ^{[V,W]}[(OH)_{2.75(9)}O_{1.25(9)}]$;

core: $^{[X]}(Na_{0.84(2)}\square_{0.16(2)})\ ^{[Y]}(Al_{3.00(0)})\ ^{[Z]}(Al_{5.97(4)}Si_{0.03(3)})\ ^{[T]}(Si_{3.45(24)}B_{2.53(25)}Al_{0.03(3)}O_{18})$ $(BO_3)_3\ ^{[V,W]}[(OH)_{3.68(23)}O_{0.32(23)}]$.

OH content was calculated based on charge balance requirements. Compositional data are summarized in Table 1 and Fig. 3.

The columnar and acicular tourmalines are chiefly solid solutions between the hypothetical endmember olenite [$NaAl_3Al_6Si_6O_{18}(BO_3)_3O_3(OH)$] and X-site-vacant Al-tourmaline [$\square Al_3Al_6Si_6O_{18}(BO_3)_3O_2(OH)_2$] (Wodara and Schreyer 2001). The small amount of calculated octahedral $^{[Z]}$Si might be insignificant considering the range of error. However, small amounts of $^{[Z]}$Si have also been suggested for synthetic tourmaline from other high-*P* studies (Schreyer et al. 2000; Berryman et al. 2014; Wunder et al. 2015). The amount of excess B significantly varies between the columnar crystals (1.18(15) $^{[4]}$B pfu) and core (2.53(25) $^{[4]}$B pfu) and rim (1.43(15) $^{[4]}$B pfu) of the acicular crystals. Cores of the acicular tourmalines have the highest B concentration ever detected in synthetic or natural tourmalines. The mechanism of $^{[4]}$B incorporation into the synthetic olenitic tourmaline is discussed below.

Natural Koralpe tourmaline. The natural tourmalines are generally of olenitic composition with a small schorl component, which is higher in the core than in the rim (Table 1). B contents vary from 3.33(6) B pfu in the core to 3.67(12) B pfu in the rim (Table 1). Both the major element composition and the total B concentrations perfectly reproduce the compositional range found in previous studies that used a combination of single-crystal X-ray diffraction, EMP, and SIMS analyses (Hughes et al. 2004; Kalt et al. 2001). This confirms the reliability of our EMPA, particularly for the determined B concentrations.

Single-crystal X-ray structure refinement (SREF) of synthetic columnar tourmaline

The lattice parameters of the synthetic columnar tourmaline are a = 15.613(5), c = 7.043(2) Å, V = 1486.8(8) Å^3 (Table 2). Compared to the results of the powder XRD, the length of the a axis is slightly smaller, whereas the c axis is slightly larger. However, the resulting unit cell volume derived from the SREF is higher than the one from the powder XRD (1485.7(2) Å^3) pointing to lower $^{[4]}$B concentrations in the columnar crystal (Ertl et al. 2012), which is in line with the EMPA (Table 1). As the mixture used for the powder XRD contained both, $^{[4]}$B rich acicular tourmaline and $^{[4]}$B poor columnar crystals, the resulting unit cell volume is slightly smaller.

Final atomic coordinates, displacement parameters and site-occupancy factors are given in Table 3 and selected interatomic distances in Table 4. The single-crystal X-ray structure refinement of the investigated synthetic tourmaline crystal results in the following formula (Table 1):

$^{[X]}(Na_{0.58(1)}\square_{0.42(1)})\ ^{[Y]}(Al_{2.83(1)}\square_{0.17(1)})\ ^{[Z]}(Al_{6.00})\ ^{[T]}(Si_{4.6(1)}B_{1.4(1)}O_{18})$

$(BO_3)_3\ ^{[V]}(OH)_3{}^{[W]}(O_{0.66(4)}OH_{0.34(4)})$.

Compared with the EMPA-derived concentrations (Table 1), the refinement of site occupancies indicates a similar $^{[4]}$B content. Hence, this synthetic tourmaline crystal has the highest refined $^{[4]}$B content ($B_{1.4(1)}$; Table 3) compared to all other published SREF of natural or synthetic tourmalines (*e.g.*, Ertl et al. 1997, 2012). There is no clear indication of presence of octahedral $^{[Z]}$Si and of tetrahedral $^{[T]}$Al from the refinements alone. Contrary to the formula calculated from EMPA, a small number of Y site vacancies were identified from the refinement (Table 3). The mean <Y-O> distance with 1.930(1) Å and the mean <T-O> distance with 1.587(1) Å (Table 4) are by far the smallest distances ever derived from a SREF.

For a fully occupied V site by 3 OH, the bond-angle distortion of the ZO_6 octahedron ($^{Z}\sigma_{oct}^{2}$) is linearly correlated to the <Y-O> distance (Ertl et al. 2005). Our structural refinement results in $^{Z}\sigma_{oct}^{2}$ = 58.9 and mean <Y-O> = 1.930(1) Å; these values plot only slightly away from the linear correlation (Ertl et al. 2005). Thus, we assume 3 OH at the V site and by charge balance, the W site occupancy was calculated to be $[O_{0.66(4)}(OH)_{0.34(4)}]$ (Table 2).

Single-crystal Raman spectroscopy

Synthetic tourmaline. EMPA indicated that $^{[4]}$B concentrations decrease significantly from core to rim of the acicular tourmaline. Columnar tourmalines have the smallest but more homogeneously distributed $^{[4]}$B concentrations (Table 1). A main goal of our study was to clarify whether changes in $^{[4]}$B concentrations can be detected with Raman spectroscopy in the OH-stretching region. To test this hypothesis we recorded Raman spectra with the electric field vector, E, parallel and perpendicular to the *c* axis (E ∥ *c* and E ⊥ *c,* respectively) of the columnar tourmaline and of the core and rim regions of acicular tourmaline. Only grains big enough to accommodate the rather large Raman spot (3 - 5 μm) were chosen for the measurements. Since the acicular tourmaline aggregates are generally smaller, we found only one crystal for which it was ensured that the scattered light is exclusively derived from the B rich core region (Fig. 4a). We also acquired another spectrum from the corresponding rim (Fig. 4b), and also spectra in each rim of three additional acicular crystals (4 spectra altogether). For the columnar crystals we measured two grains at points halfway between the +*c* and –*c* poles and another grain directly at the +*c* and –*c* poles (4 spectra). A representative Raman spectrum of a columnar crystal is shown in Fig. 4c. Exact band positions, relative integral intensity (I_{rel}) and FWHM are summarized in Table 5a. In all spectra the intensity is distributed over six bands within three frequency regions, which are clearly separated from each other.

The low-frequency region (3000 - 3400 cm^{-1}) comprises two bands centered at 3284 - 3301 cm^{-1} (ν1) and 3367 - 3370 cm^{-1} (ν2), the latter generally being the more intense. The ν1 band is visible as a shoulder at the low energy side of the ν2 band in the spectrum of the columnar crystal (Fig. 4c) and fades into a tailing to lower wavenumbers in the spectrum of the acicular core (Fig. 4a). The sum of the relative intensities of ν1 and ν2 is highest in the core of the acicular crystal (58%) and lowest in the columnar crystals (43%). For the latter, only small variations exist between different grains. Concurrently, different spot positions inside a single grain yielded similar intensity sums for ν1 and ν2. Spectra from the rim of the acicular crystals show large variations (Table 5a, Fig. 4b) but have intermediate values on average (51%).

The mid-frequency region (3400 - 3550 cm^{-1}) consists of two bands at 3451 - 3458 cm^{-1} (ν3) and 3498 cm^{-1} (ν4), which combine to higher intensities than the ν1 and ν2 bands in the columnar crystals (54%), whereas they are less intense in the core of the acicular crystal (40%). Again, the rims of the acicular tourmalines show intermediate values (46%) but also a large scatter.

The high-frequency region (3550 - 3800 cm^{-1}) shows the lowest intensity bands in all measurements (1-2 %). A small separate band at 3554 - 3556 cm^{-1} (ν5) appears in the columnar crystal spectra (Fig. 4b), whereas in the cores of the acicular crystals the contribution of the same band leads to a little tailing of ν4 towards higher wavenumbers. All tourmaline domains also contain an isolated band at 3601 – 3603 cm^{-1} (ν6).

If E is perpendicular to the *c*-axis, all bands have a much lower intensity. The reduction is most pronounced for the bands at the low- and the mid-frequency regions (90 - 100%). The ν6-band only loses 40 - 60% of intensity (Fig. 4).

Natural Koralpe tourmaline. Raman spectra of the natural tourmaline were acquired at three different spots in the $^{[4]}$B rich rims (Fig. 4d) and three spots in the $^{[4]}$B poor cores (Fig. 4e). Compared to the synthetic tourmalines, the Raman spectra are much more complex. In total 11 bands were needed to yield an adequate fit ($r^2 = 0.999$). Results of the fitting were averaged and compiled in Table 5b.

In the *low frequency region* only one band appears at 3385 - 3390 cm^{-1}, corresponding to the ν2 band in the spectra of the synthetic crystals with a slight shift of ~20 cm^{-1} to higher wavenumbers. Its relative integrated intensity in the $^{[4]}$B rich rim (22%) is higher than in the B-poor core (14%).

The *mid frequency region* contains two bands at 3462 - 3471 cm^{-1} and 3517 - 3522 cm^{-1}. Their positions coincide with the locations of the ν3 and ν4 band of the synthetic crystals by tolerating a ~20 cm^{-1} wavenumber shift to higher energies. About half of the integrated intensity is accommodated by the ν3 band (47 - 50%), whereas the ν4 band is less intense (10 - 17%) and appears as a shoulder of the ν3 feature (Fig. 4d, e).

The *high frequency region* is made up of six bands. Although two bands at 3551 - 3562 cm^{-1} and 3597 - 3601 cm^{-1} appear to correspond to the ν5 and ν6 bands in the synthetic crystals, their relative intensities are about an order of magnitude higher. Hence, we decided to assign them as ν7 and ν8, respectively. This will be justified by the Raman band assignment below. Another four low intensity bands (~1% each) are observed at 3641 - 3653 cm^{-1} (ν9), 3666 - 3668 cm^{-1} (ν10), 3675 - 3677 cm^{-1} (ν11), 3682 - 3703 cm^{-1} (ν12). None of those were detected in the Raman spectra of the synthetic tourmaline crystals.

It is important to note that the low frequency band at about 3370 cm^{-1} (ν2) shows up in each of our spectra. Its position is compatible with the IR-band, which Schreyer et al. (2000) attributed to the occurrence of $^{[4]}$B in synthetic olenitic tourmaline (3367 cm^{-1}). We will show

later that the sum of the relative integrated intensities of the two low frequency bands (ν1 and ν2) correlates with the amount of $^{[4]}$B measured by EMP (see Fig. 5, below). Band-assignments will also be discussed below (see Table 6, below).

DISCUSSION

For the scope of our study of an unambiguous band assignment, it is crucial to reliably determine B contents with the EMPA. The results of our EMPA with a single crystal structural refinement of a synthetic columnar crystal, are in good agreement (Table 1). It is clear that this is only possible because our tourmalines are significantly larger than the synthetic $^{[4]}$B-bearing tourmaline presented by Schreyer et al. (2000), which rarely exceeded 1 μm (their Fig. 2). As a second test we compare our EMPA of the natural Koralpe tourmaline with the chemical characterizations in Hughes et al. (2004) and Kalt et al. (2001), whose results are also in good agreement with our data. Hence, we are confident that our B quantifications by EMPA are sufficiently accurate. Concurrently, the small beam diameter of 2 μm allows for spatial correlation of $^{[4]}$B concentrations with the according Raman signal, which is a pre-requisite for the reliable interpretation of the Raman spectra.

Mechanism of $^{[4]}$B incorporation into synthetic olenitic tourmaline

Olenite with the endmember structural formula, $NaAl_3Al_6Si_6O_{18}(BO_3)_3O_3(OH)$, has a large H deficit compared to other members of the tourmaline supergroup, which allows excess B to be incorporated via the coupled substitution

(1) $^{[T]}Si_{-1}\,^{[V]}O_{-1}\,^{[T]}B_1\,^{[V]}OH_1$.

$^{[4]}$B incorporation in our synthetic tourmaline is mainly due to this exchange vector (Fig. 3). Based on bond valence considerations (Hawthorne 2002) the maximum amount of excess B that

can be incorporated by substitution (1) is two $^{[4]}$B pfu given that the Y and Z sites are completely occupied by Al. However, the synthetic high-*P* tourmalines described by Wodara (1996) and that of our study have more than two $^{[4]}$B pfu. Secondly, Marschall et al. (2004) reported on excess B in natural dravitic tourmaline (~0.26 $^{[4]}$B pfu). Hence, additional mechanisms must be present with

(2) $^{[T]}Si_{-1}\ ^{[Z]}Al_{-1}\ ^{[T]}B_{1}\ ^{[Z]}Si_{1}$

(3) $^{[X]}\square_{-1}\ ^{[T]}Si_{-1}\ ^{[X]}Na_{1}\ ^{[T]}B_{1}$.

being the most likely. Our data show a positive correlation of Na pfu and B pfu, which suggests that substitution (3) is effective (Fig. 3b), thus pointing to a co-occurence of Na at the X site and B at the T site. Such a coupling is reasonable as substituting B^{3+} for Si^{4+} provides a charge deficit that is compensated with Na on the X site. However, by synthesizing an X-vacant olenite with excess B, Wodara and Schreyer (2001) have shown that occupancy of the X site is not a pre-requisite for the incorporation of $^{[4]}$B and it is unclear how much of the $^{[4]}$B is incorporated by substitution (3) as Na could as well enter the structure via the B-absent exchange $^{[X]}\square_{-1}\ ^{[V,W]}(OH)_{-1}\ ^{[X]}Na_{1}\ ^{[V,W]}O_{1}$. To solve this problem, accurate and independent determinations of the water concentrations are needed.

With regard to substitution (2), a linear anti-correlation of Al and B was not detected within errors of the EMPA. This is in line with the observation that the single-crystal XRD refinement does not show significant $^{[Z]}$Si to be present, and that the amount of $^{[Z]}$Si determined by EMPA is insignificant within analytical errors. We conclude that if coupled substitution (2) is present at all, it only subordinately contributes to the incorporation of $^{[4]}$B.

Because the main mechanism for the incorporation of $^{[4]}$B is exchange vector (1), tourmalines with the highest B concentrations should have the highest OH contents. It is well-known that the total integrated Raman intensity (I_{tot}) in the OH-stretching region linearly

correlates with the OH content (*e.g.*, MacMillan and Hofmeister 1988). Therefore, I_{tot} in the frequency region 2800 - 4000 cm^{-1} should display a positive linear correlation with the B concentrations. I_{tot} of our Raman spectrum of the B rich core of the acicular crystal is about 20% higher than that of the B poor columnar crystal (Fig. 4a, c), thus confirming exchange vector (1) as dominant $^{[4]}B$ incorporation mechanism into tourmaline.

Chemical zoning of the acicular tourmalines

We interpret the outermost rims of the acicular crystals and the columnar crystals to be in equilibrium with the final fluid at experimental *P-T* conditions. Core compositions are likely to be metastable and are presumably caused by rapid tourmaline growth during heating and/or chemical changes in the coexisting solution during growth (see Berryman 2015a, b).

Raman band assignment

Influence on frequency of OH-stretching vibration in tourmaline. In tourmaline, H bonding occurs at the two crystallographic sites V (with O3) and W (with O1). Bands associated with (O1)H-stretching vibrations always have the highest frequencies as the distance O1-H is smaller than the distance O3-H (Gatta et al. 2014). Local arrangement of cations around the two proton-accepting oxygens further affects the strength of the OH bonds. (O3)H groups are surrounded by two Z and one Y cation (YZZ configuration) and (O1)H by three Y cations (YYY configuration). The higher the sum of the charge of the Y and Z cations the lower the frequency of the associated OH-stretching vibration (Gonzalez-Carreño et al. 1988).

A second order effect on band position is caused by hydrogen bridge bonding between (O3)H groups and the O5 ion in the T_6O_{18} ring. The stronger the O3-H…O5 bond, the weaker the O3-H bond. Substituting Al^{3+} for Si^{4+} on the T site shifts the (O3)H band up to 50 cm^{-1} towards

lower frequencies (Gourdant et al. 1997) because trivalent Al lowers the negative charge of the O5 and therefore strengthens the O3-H…O5 hydrogen bridge bond. Concurrently, O1-H…O5 and O1-H…O4 hydrogen bridge bonding are considered as absent or very weak (Skokby et al. 2012).

A third order effect is caused by the occupancy of the X site by Na^{+}, K^{+} or Ca^{2+}, reducing the charge of the O5, such that O3-H…O5 bonds are weakened and the frequency of the (O3)H-stretching vibration shifts to higher energies. In comparing synthetic Mg-foitites and dravites this results in a splitting of up to 50 cm^{-1} between the $^{[X]}\square$ - $^{[Y]}Al^{[Z]}Al^{[Z]}Al$ - $^{[T]}Si/Si$ and $^{[X]}Na$ - $^{[Y]}Al^{[Z]}Al^{[Z]}Al$ - $^{[T]}Si/Si$ species (Veličkov, 2002). Similarly, charge and ionic radius of the cation at the X site affects the strength of the O1-H bond due to repulsive interaction with the positively charged H. If K^{+} substitutes for the smaller Na^{+} ion in synthetic dravites, a shift of about 20 cm^{-1} to higher frequencies of the (O1)H band occurs (Berryman et al. 2015a).

The sum of the effects produces a pattern of several Raman bands, whose relative intensities give a measure for the abundance of the associated cation arrangements and directly reflect tourmaline chemistry.

Synthetic tourmaline. The advantage of assigning Raman bands to the spectra of our synthetic olenitic tourmalines is that only Al is present at the octahedral sites. Therefore, all bands relate to either $^{[Z]}Al^{[Z]}Al^{[Y]}Al$ or $^{[Y]}Al^{[Y]}Al^{[Y]}Al$ environments. Vacancies at the Y site or Si at the Z site are insignificant. Moreover, since Al as a tetrahedral occupant is rare or even absent, only $^{[4]}Si/Si$ and $^{[4]}Si/B$ species exert a significant contribution to the Raman signal. B as a trivalent cation should generally cause a shift to lower wavenumbers. Compared to Al on the T site, the shift should be much more pronounced as in an undistorted tetrahedron B-O distances (1.48 Å) are smaller then Al-O distances (1.70 Å). The core of the acicular crystal is highest in B and shows the highest intensity in the low-frequency region (Fig. 4, Table 5). Therefore, we

conclude that the bands ν1 and ν2 in the low frequency region are associated with $^{[T]}$Si/B species in the tetrahedral ring (Table 6). This is in agreement to the assignment of the 3367 cm^{-1} IR-band to $^{[4]}$B by Schreyer et al. (2000). Probably due to the potential contribution of molecular water in their KBr pellet Schreyer et al. (2000) precluded that there is a second band (ν1), which indeed derives from tourmaline. The two bands ν3 and ν4 in the mid frequency region belong to the $^{[T]}$Si/Si configuration (Table 6), with the expected large shift of 130 - 150 cm^{-1} to higher wavenumbers compared to the $^{[T]}$Si/B species.

The band splitting in the low (70 cm^{-1}) and mid frequency regions (50 cm^{-1}) is probably caused by mixed □/Na occupancy on the X site. Within $^{[T]}$Si/B species the shift is higher by about 20 cm^{-1}, which is most likely due to the decrease of <X-O5> distances once B is present in the tetrahedral ring. This is supported by the fact that average <X-O5> distances in the columnar crystal are significantly smaller (2.65 Å, Table 4) compared to a natural olenite devoid of $^{[4]}$B (2.72 Å, Cempírek et al. 2006). The intensity ratio of $^{[X]}$Na - $^{[T]}$Si/B (ν2) / $^{[X]}$□ - $^{[T]}$Si/B (ν1) is considerably higher than that of $^{[X]}$Na - $^{[T]}$Si/Si (ν4) / $^{[X]}$□ - $^{[T]}$Si/Si (ν3), which might argue for ordering of $^{[X]}$Na and $^{[T]}$Si/B species.

The high frequency region has the lowest intensities, thus bands are assigned to (O1)H-stretching vibrations. We assign the ν5 band to the $^{[X]}$□ - $^{[Y]}$Al$^{[Y]}$Al$^{[Y]}$Al, and the ν6 band to the $^{[X]}$Na - $^{[Y]}$Al$^{[Y]}$Al$^{[Y]}$Al configuration (Table 6). The splitting of 50 cm^{-1} is compatible with observations in synthetic dravites (Gourdant et al. 1997).

Natural Koralpe tourmaline. Due to additional occupants (*e.g.,* Fe, Li and □ on Y; Al on T; Ca on X) band assignment is more difficult. However, the most abundant occupant of the Y site is Al, of the T site Si and B, and of the X site Na (Table 1; see also Kalt et al. 2001; Hughes et al. 2004). Hence, it is possible to assign some of these bands by comparison with that of our synthetic tourmalines. We found energetic coincidence between 3 bands, namely of ν2, ν3, and

ν4. Band ν3 at 3462 - 3471 cm^{-1} is the most intense and therefore must correspond to the most abundant configuration, which is $^{[Y]}Al^{[Z]}Al^{[Z]}Al$ - $^{[T]}Si/Si$ - O3 - $^{[X]}\square$. The $^{[X]}Na$ equivalent (ν4) is present at 50 cm^{-1} towards higher wavenumbers, as deduced from the assignment of the synthetic tourmaline spectra (Table 5a). The broad band at 3385 - 3390 cm^{-1} (ν2) belongs to $^{[Y]}Al^{[Z]}Al^{[Z]}Al$ - $^{[T]}Si/B$ - O3 - $^{[X]}Na$. Considering the large shift to lower wavenumbers, this band must involve $^{[4]}B$, also because the intensity decreases towards the B-poorer rim (Fig. 4). The X-vacant equivalent (ν1) is not sufficiently intense to be detected in any of the Koralpe spectra, probably due to the combined effect of $^{[X]}Na$ - $^{[T]}Si/B$ ordering, low abundance of vacancies and lower $^{[4]}B$ concentrations. All three bands are systematically shifted by 20 cm^{-1} to higher energies, which is interpreted by the accumulation of various small structural differences between synthesized and natural tourmalines.

Assignment of bands ν7 - ν12 is rather tentative as we just have a qualitative understanding of the interaction between other occupants and band positions. For example, for an (O3)H-stretching vibration (in an otherwise similar environment) the $^{[Y]}Fe^{2+[Z]}Al^{[Z]}Al$ arrangement (Σ = 8+) should cause a band at higher energies compared to the $^{[Y]}Al^{[Z]}Al^{[Z]}Al$ arrangement (Σ = 9+), and at lower energies compared to the possible $^{[Y]}Li^{[Z]}Al^{[Z]}Al$ cluster (Σ = 7+). Furthermore, Ca^{2+} on the X site should cause an even more pronounced shift to higher wavenumber than Na^{+}. Moreover, some bands might also derive from superposition of two or more bands, precluding clear band separation. For example, band ν6 (3601 - 3603 cm^{-1}) in the spectra of the synthetic crystals corresponds to an (O1)H-stretching vibration with Na on the X site. Its relative intensity is 1-2 %. In the spectra of the natural Koralpe tourmaline a band at the same position (3597 - 3601 cm^{-1}) shows up, but its relative intensity is much higher (6 - 9 %), whereas Na contents are even lower than in all of the synthetic tourmalines (Table 1). Therefore, it is likely that a second band is superimposed, so we introduce a new band ν8 at the same

position as ν6. To infer its most likely cation configuration two boundary conditions are important: the sum of the cation charge (Σ) must be below 9+ and the configuration based on the chemistry must be sufficiently abundant. Taking this into account, we assigned the band ν8 to the $^{[Y]}Li^{[Z]}Al^{[Z]}Al$ configuration around the (O3)H group. Following this logic, we introduced the band ν7 superimposing ν5 , which is possibly associated with the $^{[Y]}Fe^{2+[Z]}Al^{[Z]}Al$ configuration. Supporting this assignment, the relative intensity ratio of ν8 (Li-related) over ν7 (Fe-related) increases from the core (0.5) to the rim (1.5), if the contributions of the underlying low intensity bands ν6 and ν5 are disregarded. This is in agreement with the increase of $^{[Y]}Li/^{[Y]}Fe^{2+}$ ratios from core to rim determined by Hughes et al. (2004).

Bands ν9 - ν12 are presumably related to the (O1)H-stretching vibration due to their low intensities. Skogby et al. (2012) recognized a band at 3657 - 3658 cm^{-1} in a Raman spectrum of a natural elbaite and assigned it to a $^{[Y]}Li^{[Y]}Al^{[Y]}Al$ environment around (O1)H. Hence, as these positions are close, we assign the bands ν9 (3641 - 3653 cm^{-1}) and ν10 (3666 - 3668 cm^{-1}) to $^{[Y]}Li^{[Y]}Al^{[Y]}Al$ with either Na^{+} (ν9) or Ca^{2+} (ν10) on the X site. The two outermost bands possibly correspond to the $^{[Y]}\square^{[Y]}Al^{[Y]}Al$ - Na (ν11) and $^{[Y]}\square^{[Y]}Al^{[Y]}Al$ - Ca (ν12) arrangement. Both, the occurrence of Li and □ on the Y site in the Koralpe tourmaline has been confirmed by Ertl et al. (1997), Kalt et al. (2001) and Hughes et al. (2004).

Correlation of $^{[4]}B$ concentration and intensity of low frequency OH bands

The sum of the relative integral area (I_{rel}) of the $^{[4]}B$-related bands (ν1, ν2) strongly increases with the $^{[4]}B$ concentrations (EMPA-data; Fig. 5) Fitting a regression line through the origin and assuming that I_{rel} (ν1) + I_{rel} (ν2) = 0 if no $^{[4]}B$ is present, this results in the following correlation within a 95% confidence interval:

$$^{[4]}B\left[\text{pfu}\right]=0.03(1)\cdot\left[I_{rel}\left(\nu1\right)+I_{rel}\left(\nu2\right)\right]$$

At the same time, to the best of our knowledge none of the published IR or Raman spectra of $^{[4]}$B free tourmalines contain the ν1 and/or the ν2 bands (so far our attempts to synthesize $^{[4]}$B free olenite failed). In summary this means, that if the Raman spectrum of any unknown tourmaline contains the ν1 and/or the ν2 band, $^{[4]}$B will definitely be present in the tourmaline structure. This is also valid for tourmalines with compositions deviating from the olenite endmember as long as they contain a substantial olenitic component, i.e. as long as they contain sufficient clusters with $^{[Y]}$Al$^{[Z]}$Al$^{[Z]}$Al configurations around the O3-H bond.

While Al is the only occupant on the Z site in the core of the Koralpe tourmaline, only 64% of the Y site are occupied by Al, the reminder being Fe^{2+} (31%), Mg^{2+}(4 %) and Ti^{4+} (1%); Table 1). Despite the large schorl component, the ν2 band at 3384 cm^{-1} is maintained in the Raman spectrum (Fig. 4e). Berryman et al. (2015b) presented a Raman spectrum of synthetic dravite with ~ 0.7 $^{[4]}$B pfu and along with a $^{[Y]}$Al$^{[Z]}$Al$^{[Z]}$Al abundance of 31% (their Table 7a), which exhibits a band at 3381 cm^{-1} that can be attributed to the presence of $^{[4]}$B (their Figure 5, sample EB28). Similarly, infrared spectra of liddicoatites-elbaites from Anjanabonoina, Madagascar with ~ 0.4 $^{[4]}$B pfu and a $^{[Y]}$Al$^{[Z]}$Al$^{[Z]}$Al abundance of 60% (Ertl et al. 2006, their Figure 4) show a band between 3300-3400 cm^{-1}, which is likely associated with $^{[4]}$B.

However, reduced abundance of $^{[Y]}$Al$^{[Z]}$Al$^{[Z]}$Al clusters lowers the detection limit for $^{[4]}$B as lower valent substitutes as Li^{+}, Mg^{2+} or Fe^{2+} on either Y or Z sites transfer some intensity of the ν1 and/or ν2 towards higher frequencies. These bands might not be resolvable as more intense bands are likely superimposed at the same frequency. This implies that the absence of ν1 and/or the ν2 bands does not a priori preclude the presence of $^{[4]}$B, especially if the olenitic component is very low. For those tourmalines, our approach will solely serve as a qualitative indicator for $^{[4]}$B, with a detection limit that depends, besides the quality of the Raman spectra, on the chemistry of the tourmalines. K-dravite synthesized by Berryman et al. (2015a) contains ~ 0.25 $^{[4]}$B pfu

(EMPA data) and neither ν1 or ν2 shows up in the single crystal Raman spectra (Berryman et al. 2015b, their figure 5). Yet, for more Al-rich tourmalines we are confident that a $^{[4]}$B content of > 0.3 $^{[4]}$B will easily be detectable by Raman spectroscopy.

IMPLICATIONS

Most Raman spectroscopic studies have been conducted on natural tourmaline, which are generally solid solutions of multiple endmembers, which leads to complicated Raman spectra, hindering unambiguous band assignment. In our study, we have shown that polarized Raman spectroscopy can be used as a method to distinguish between different cation arrangements and hence, tourmaline compositions. However, reliable band assignment is only possible by using synthetic, chemically well-characterized tourmalines of rather simple composition. Further Raman studies on synthetic endmember tourmalines are needed for constructing a comprehensive database, which will promote Raman spectroscopy as a non-destructive method for the chemical classification of (precious) natural tourmaline. Moreover, it will serve as a fast and straightforward tool to characterize chemical zonation of tourmalines in thin sections of several rock types. Abandoning spatial resolution, the results of our study are also applicable to powder samples, although it must be ensured that no other OH-bearing phases are present.

ACKNOWLEDGEMENTS

We thank H.-P. Nabein for generating the XRD patterns and U. Dittmann for EMP sample preparation. E. Berryman is acknowledged for native speaker proof-reading. This study was supported by funding from the Deutsche Forschungsgemeinschaft granted to GF and WH (FR

557/31-1; HE 2015/16-1) and by the Austrian Science Fund (FWF) project no. P-26903-N19. We thank the associate editor Hans-Peter Schertl, Andrey Korsakov and an anonymous reviewer for their constructive comments.

REFERENCES CITED

Armstrong, J.T. (1995) CITZAF: a package of correlation programs for the quantitative electron microbeam X-ray analysis of thick polished materials, thin films, and particles. Microbeam Analysis, 4, 177-200.

Bastin, G.F., and Heijligers, H.J.M. (1990) Quantitative electron-probe microanalysis of ultralight elements (boron-oxygen). Scanning, 12, 225-236.

Bast, R., Scherer, E.E., Mezger, K., Austrheim, H., Ludwig, T., Marschall, H.R., Putnis, A., and Löwen, K. (2014) Boron isotopes in tourmaline as a tracer of metasomatic processes in the Bamble sector of Southern Norway. Contributions to Mineralogy and Petrology, 168, 1069.

Berryman, E.J., Wunder, B., and Rhede, D. (2014) Synthesis of K-dominant tourmaline. American Mineralogist, 99, 539-542.

Berryman, E.J., Wunder, B., Wirth, R., Rhede, D., Schettler, G., Franz, G., and Heinrich, W. (2015a) An experimental study on K and Na incorporation in dravitic tourmaline and insight into the origin of diamondiferous tourmaline from the Kokchetav Massif, Kazakhstan. Contributions to Mineralogy and Petrology, 129:28.

Berryman, E.J., Wunder, B., Ertl, A., Koch-Müller, M., Rhede, D., Scheidl, K., Giester, G., and Heinrich, W. (2015b) Investigation of synthetic K-dravite, dravite, oxy-uvite, and

magnesio foitite using SREF and Raman spectroscopy. Physics and Chemistry of Minerals, in review.

Cempírek, J., Novák, M., Ertl, A., Hughes, J.M., Rossman, G.R., and Dyar, M.D. (2006) Fe-bearing olenite with tetrahedrally coordinated Al from an abyssal pegmatite at Kutná Horza, Czech Republic: Structure, crystal chemistry, optical and XANES spectra. The Canadian Mineralogist, 44, 23-30.

Clark, C.M., Wadoski, E.R., and Freeman, E.D. (2008) Tourmaline chemistry and the ^{III}B site. American Mineralogist, 93, 409-413.

Ertl, A., and Brandstätter, F. (1998) Olenit mit Borüberschuß in einem Metapegmatit östlich der Stoffhütte, Koralpe, Steiermark, Österreich. Mitteilung der Abteilung für Mineralogie am Landesmuseum Joanneum, 62/63, 3-21.

Ertl, A., Giester G., Ludwig, T., Meyer, H.P., and Rossman, G.R. (2012) Synthetic B-rich olenite: Correlations of single-crystal structural data. American Mineralogist, 97, 1591-1597.

Ertl, A., Hughes, J.M., Prowatke, S., Ludwig, T., Brandstätter, F., Körner, W., and Dyar, M.D. (2007) Tetrahedrally coordinated boron in Li-bearing olenite from „mushroom“ tourmaline from Momeik, Myanmar. The Canadian Mineralogist, 45, 891-899.

Ertl, A., Hughes, J.M., Prowatke, S., Ludwig, T., Prasad, P.S.R., Brandstätter, F., Körner, W., Schuster, R., Pertlik, F., and Marschall, H. (2006) Tetrahedrally coordinated boron in tourmaline from the liddicoatite-elbaite series from Madagascar: Structure, chemistry, and infrared spectroscopic studies. American Mineralogist, 91, 1847-1856.

Ertl, A., Pertlik, F., and Bernhardt, H.-J. (1997) Investigations on olenite with excess boron from the Koralpe, Styria, Austria. Anzeiger Abt. I, 124, 3-10.

Ertl, A., Rossman, G.R., Hughes, J.M., Prowatke, S., and Ludwig, T. (2005) Mn-bearing „oxy-rossmanite“ with tetrahedrally coordinated Al and B from Austria: Structure, chemistry, and infrared and optical spectroscopic study. American Mineralogist, 90, 481-487.

Ertl, A., Tillmanns, E., Ntaflos, T., Francis, C., Giester, G., Körner, W., Hughes, J.M., Lengauer, C., and Prem, M. (2008) Tetrahedrally coordinated boron in Al-rich tourmaline and its relationship to the pressure-temperature conditions of formation. European Journal of Mineralogy, 20, 881-888.

Fantini, C., Tavares, M.C., Krambrock, K., Moreira, R.L., and Righi, A. (2014) Raman and infrared study of hydroxyl sites in natural uvite, fluor-uvite, magnesio-foitite, dravite and elbaite tourmalines. Physics and Chemistry of Minerals, 41, 247-254.

Fischer, R.X., and Tillmanns, E. (1988) The equivalent isotropic displacement factor. Acta Crystallographica, C44, 775-776.

Gatta, G.D., Bosi, F., McIntyre, G.J., and Skogby, H. (2014) First accurate location of two proton sites in tourmaline: A single-crystal neutron diffraction study of oxy-dravite. Mineralogical Magazine, 78(3), 681-692.

Gonzalez-Carreño, T., Fernandez, M., and Sanz, J. (1988) Infrared and electron microprobe analysis of tourmalines. Physics and Chemistry of Minerals, 15, 452-460.

Gourdant , J.P., Robert, J.-L., and Sanz, J. (1997) Tetrahedrally coordinated aluminium in synthetic tourmalines. In Tourmaline 1997 symposium, Abstract volume, Nové Mesto na Morave, Czech Republic, p. 29.

Hawthorne, F.C. (1996) Structural mechanisms for light-element variations in tourmaline. The Canadian Mineralogist, 34, 123-132.

Hawthorne, F.C. (2002) Bond-valence constraints on the chemical composition of tourmaline. The Canadian Mineralogist, 40, 789-797.

Henry, D.J., and Dutrow, B.L. (1996) Metamorphic tourmaline and its petrological application. Reviews in Mineralogy, 33, 503-557.

Henry, D.J., Kirkland, B.L., and Kirkland, D.W. (1999) Sector-zoned tourmaline from the cap rock of a salt dome. European Journal of Mineralogy, 11, 263-280.

Henry D.J., Novak, M., Hawthorne, F.C., Ertl, A., Dutrow, B.L., Uher, P., and Pezzotta, F. (2011) Nomenclature of the tourmaline-supergroup minerals. American Mineralogist, 96, 895-913.

Hughes, J.M., Ertl, A., Dyar, M.D., Grew, E., Shearer, C.K., Yates, M.G., and Guidotti, C.V. (2000) Tetrahedrally coordinated boron in a tourmaline: Boron-rich olenite from Stoffhütte, Koralpe, Austria. The Canadian Mineralogist, 38, 861-868.

Hughes, J.M., Ertl, A., Dyar, M.D., Grew, E., Wiedenbeck, M., and Brandstätter F. (2004) Structural and chemical response to varying $^{[4]}$B content in zoned Fe-bearing olenite from Koralpe, Austria. The Canadian Mineralogist, 38, 447-454.

Hughes, K.-A., Hughes, J.M., and Dyar, M.D. (2001) Chemical and structural evidence for $^{[4]}$B $\Leftrightarrow$ $^{[4]}$Si substitution in natural tourmalines. European Journal of Mineralogy, 13, 743-747.

Kalt, A., Schreyer, W., Ludwig, T., Prowatke, S., Bernhardt, H.-J., and Ertl, A. (2001) Complete solid solution between magnesian schorl and lithian excess-boron olenite in a pegmatite from the Koralpe (eastern Alps, Austria). European Journal of Mineralogy, 13, 1191-1205.

Kowalski, P.M., Wunder, B., and Jahn, S. (2013) Ab initio prediction of equilibrium boron isotope fractionation between minerals and aqueous fluids at high *P* and *T*. Geochimica et Cosmochimica Acta, 101, 285-301.

Krosse, S. (1995) Hochdrucksynthese, Stabilität und Eigenschaften der Borosilikate Dravit und Kornerupin sowie Darstellung und Stabilitätsverhalten eines neuen Mg-Al-Borates. Dissertation, Ruhr-Universität Bochum, Germany, 135 pp.

Larson, A.C., and Von Dreele, R.B. (1987) Generalized structure analysis system. Los Alamos National Laboratory Report LA-UR-86-748.

Lussier, A.J., Aguiar, P.M., Michaelis, V.K., Kroeker, S., and Hawthorne, F.C. (2009) The occurrence of tetrahedrally coordinated Al and B in tourmaline: An ^{11}B and ^{27}Al MAS NMR study. American Mineralogist, 94, 785-792.

MacMillan, P.F. and Hofmeister, A.M. (1988) Infrared and Raman spectroscopy. In: Mineralogical Society of America Reviews in Mineralogy, 18, Chapter 4, p. 99-159.

Marler, B., Borowski, M., Wodara, U., and Schreyer, W. (2002) Synthetic tourmaline (olenite) with excess boron replacing silicon in the tetrahedral site: II. Structural analysis. European Journal of Mineralogy, 14, 763-771.

Marler, B., and Ertl, A. (2002) Nuclear magnetic resonance and infrared spectroscopy study of excess-boron olenite from Koralpe, Styria, Austria. American Mineralogist, 87, 364-367.

Marschall, H.R., Ertl, A., Hughes, J.M., and McCommon, C. (2004) Metamorphic Na- and OH-rich disordered dravite with tetrahedral boron associated with omphacite, from Syros, Greece: chemistry and structure. European Journal of Mineralogy, 16, 817-823.

Marschall H.R., Ludwig, T., Altherr, R., Kalt, A., and Tonarini, S. (2006) Syros metasomatic tourmaline: Evidence for high-d^{11}B fluids in subduction zones. Journal of Petrology, 47, 1915-1942.

Meyer, C., Wunder, B., Meixner, A., Romer, R.L., and Heinrich, W. (2008) Boron-isotopic fractionation between tourmaline and fluid: an experimental re-investigation. Contributions to Mineralogy and Petrology, 156, 259-267.

Mirwald, P.W., and Massonne, H.-J. (1980) Quartz-coesite transition and the comparative friction measurements in piston-cylinder apparatus using talc-alsimag-glass (TAG) and NaCl high pressure cells: a discussion. Neues Jahrbuch für Mineralogische Monatshefte, 1980, 469-477.

Miller, C. (1990) Petrology of the type locality eclogites from the Koralpe and Saualpe (Eastern Alps, Austria). Schweizerische Mineralogische und Petrographische Mitteilungen, 70, 287-300.

Miller, C., and Thöni, M. (1997) Eo-Alpine eclogitization of Permian MORB-type gabbros in the Koralpe (Eastern Alps, Austria): new geochronological, geochemical and petrological data. Chemical Geology, 137, 283-310.

Moore, J.N., Christenson, B.W., Allis, R.G., Browne, P.R.L., and Lutz, S.J. (2004) The mineralogical consequences and behaviour of descending acid-sulfate waters: an example from the Karaha-Telaga Bodas geothermal system, Indonesia. The Canadian Mineralogist, 42, 1483-1499.

Sheldrick, G.M. (1997) SHELXL-97, a program for crystal structure refinement. University of Göttingen, Germany.

Schreyer, W., Hughes, J.M., Bernhardt, H-J., Kalt, A., Prowatke, S., and Ertl, A. (2002) Reexamination of olenite from the type locality: detection of boron in tetrahedral coordination. European Journal of Mineralogy, 14, 935-942.

Schreyer, W., Wodara, U., Marler, B., van Aken, P., Seifert, F., and Robert, J.-L. (2000) Synthetic tourmaline (olenite) with excess boron replacing silicon on the tetrahedral site: I. Synthesis conditions, chemical and spectroscopic evidence. European Journal of Mineralogy, 12, 529-541.

Skogby, H., Bosi, F., and Lazor, P. (2012) Short-range order in tourmaline: a vibrational spectroscopic approach to elbaite. Physics and Chemistry of Minerals, 39, 811-816.

Strüwe, K., and Powell, R. (1995) PT paths from modal proportions: application to the Koralm Complex, Eastern Alps. Contributions to Mineralogy and Petrology, 119, 83-93.

Tagg, S.L., Cho, H., Dyar, M.D., and Grew, E.S. (1999) Tetrahedral boron in naturally occurring tourmaline. American Mineralogist, 84, 1451-1455.

Trumbull, R.B., Krienitz, M.-S., Grundmann, G., and Wiedenbeck, M. (2009) Tourmaline geochemistry and $d^{11}B$ variation as a guide to fluid-rock interaction in the Habachtal emerald deposit, Tauern Window, Austria. Contributions to Mineralogy and Petrology, 157, 411-427.

Van Hinsberg, V.J., Henry, D.J., and Marschall, H.R. (2011) Tourmaline: An ideal indicator of its host environment. The Canadian Mineralogist, 29, 1-16.

van Hinsberg, V.J., and Schumacher, J.C. (2007) Intersector element partitioning in tourmaline: a potentially powerful single crystal thermometer. Contributions to Mineralogy and Petrology, 153, 289-301.

Veličkov, B. (2002) Kristallchemie von Fe, Mg-Turmalinen: Synthese und spektroskopische Untersuchungen. Dissertation, TU Berlin, Germany, 175 pp.

von Goerne, Franz, G., and Heinrich, W. (2001) Synthesis of tourmaline solid solutions in the system Na_2O-MgO-Al_2O_3-SiO_2-B_2O_3-H_2O-HCl and distribution of Na between tourmaline and fluid at 300 to 700 °C and 200 MPa. Contributions to Mineralogy and Petrology, 141, 160-173.

Wodara, U. (1996) Synthese und Eigenschaften von Turmalinen im System Na_2O-Al_2O_3-SiO_2-B_2O_3-H_2O. Diploma thesis, Ruhr-University Bochum, Germany, 99 pp.

Wodara, U., and Schreyer, W. (2001) X-site vacant Al-tourmaline: a new synthetic end-member. European Journal of Mineralogy, 13, 521-532.

Wunder, B., Berryman, E., Plessen, B., Rhede, D., Koch-Müller, M., and Heinrich, W. (2015) Synthetic and natural ammonium-bearing tourmaline. American Mineralogist, 100, 250-256.

FIGURE CAPTIONS

Figure 1. SEM micrograph of the experimental products. Large tourmalines (Tur) appear in columnar and acicular habits. Fine-grained material consists of coesite (Coe) and small amounts of $AlBO_3$. Coesite rarely forms larger isometric crystals.

Figure 2. BSE micrograph (a) and WDX element mappings (b, c, d) showing chemical zoning of an acicular tourmaline crystal. B is enriched in the core compared to the rim. Si shows the opposite behavior**.** Concentrations of Al are rather constant across the grain, slightly enriched in the core. Two inclusions of $AlBO_3$ (dark in BSE) and one coesite inclusion (bright in BSE) are marked in (a). $AlBO_3$ shows up as dark red spots in (d, b).

Figure 3. Variations of total Si (a), Na (b) and Al (c) with total B (all given in pfu). Values calculated from EMPA of the acicular and columnar tourmalines synthesized in the piston-cylinder experiment (normalization to 18 cations on the Y, Z, T and B sites). Black squares with roman numerals mark the composition of tourmaline endmembers. Hypothetical endmembers (not yet accepted by the IMA-nomenclature commission) are denoted with (*). Variation in excess B is systematic and mainly due to coupled substitution following exchange vector $\overrightarrow{\mathrm{I, II}^*}$

(a, c). Na vs. B variations (b) are explained by a linear combination of at least two exchange vectors (dotted arrow) potentially including a coupling of Na and $^{[4]}$B via vector $\overrightarrow{\mathrm{III}^*, \mathrm{IV}^*}$. Within errors there is no correlation of Al and $^{[4]}$B, therefore contribution of exchange vector $\overrightarrow{\mathrm{I}, \mathrm{V}^*}$ is unlikely.

Figure 4. Representative single-crystal Raman spectra recorded in the frequency region of the OH-stretching vibration in the core (a) and rim (b) of a synthetic acicular crystal, a synthetic columnar crystal (c), and rim (d) and core (e) of the natural Koralpe tourmaline. Synthetic crystals were handpicked and placed on a KBr pellet. Spectra of the synthetic tourmalines were collected from the area indicated in the reflected light images. Zoned Koralpe tourmaline was probed as a polished epoxy mount. Spectra with E || *c* (top) and E $\perp$ *c* (bottom) were each acquired at the same location. $^{[4]}$B pfu concentrations are taken from the EMPA (Table 1). Gaußians marked in red are bands associated with $^{[4]}$B (for fit parameters see Table 5a, b; for band assignments see Table 6).

Figure 5. Correlation of the sum of the relative integral intensity of bands ν1 and ν2 (Raman) with the $^{[4]}$B content (EMPA). The solid line represents the linear fit assuming a regression line through the origin with the 95% confidence interval indicated with dashed lines. For the calculation we excluded the core of the Koralpe tourmaline due its low Al content on the Y site (see discussion). The regression equation is indicated in the top part of the figure and is strictly only applicable to tourmalines with olenitic composition.

TABLES

Table 1. Average chemical compositions in oxide wt% and atoms pfu of the synthetic and natural $^{[4]}$B-bearing tourmaline determined with EMPA and SREF

	Acicular grains		**Columnar crystal**		**Koralpe**	
method	EMP	EMP	EMP	SREF	EMP	EMP
position	*core*	*rim*	*center + rim*	*whole crystal*	*core*	*rim*
n	9	12	8	1	10	10
SiO_2	22.31 (1.27)	28.98 (59)	30.75 (90)	29.52*	32.22 (58)	31.72 (63)
TiO_2	n.d.	n.d.	n.d.	n.d	0.17 (5)	0.06 (4)
B_2O_3	20.58 (1.06)	16.19 (66)	15.22 (58)	16.36*	11.35 (26)	12.86 (45)
Al_2O_3	48.97 (39)	48.07 (19)	47.50 (40)	48.09*	40.02 (1.12)	45.62 (37)
FeO	n.d.	n.d.	n.d.	n.d	7.10 (1.37)	0.95 (47)
MnO	n.d.	n.d.	n.d.	n.d	0.12 (6)	0.04 (4)
MgO	n.d.	n.d.	n.d.	n.d	0.52 (9)	0.14 (12)
CaO	n.d.	n.d.	n.d.	n.d	1.12 (13)	1.55 (14)
Na_2O	2.78 (8)	2.13 (24)	1.84 (29)	2.81*	1.76 (11)	1.28 (13)
K_2O	n.d.	n.d.	n.d.	n.d.	0.03 (1)	0.01 (1)
H_2O	n.d.	n.d	n.d.	3.21*	n.d.	n.d.
Total	94.65 (20)	95.37 (56)	95.32 (40)	100	94.39 (52)	94.22 (55)
norm	*18 YZTB*	*18 YZTB*	*18 YZTB*	*none*	*18 YZTB*	*18 YZTB*
T site						
Si	3.44 (24)	4.55 (14)	4.82 (15)	4.59 (9)	5.47 (11)	5.25 (10)
$^{[4]}$B	2.53 (25)	1.43 (15)	1.18 (15)	1.41 (9)	0.33 (6)	0.67 (12)
$^{[4]}$Al	0.02 (3)	0.02 (3)	0.00 (0)	0.00	0.20 (10)	0.08 (10)
$^{[3]}$B	3.00	3.00	3.00	3.00	3.00	3.00
Y site						
Al	3.00 (0)	3.00 (0)	3.00 (0)	2.83 (1)	1.91 (31)	2.83 (10)
Fe^{2+}	n.d.	n.d.	n.d.	n.d.	0.94 (29)	0.13 (7)
Mn^{2+}	n.d.	n.d.	n.d.	n.d.	0.00 (0)	0.00 (0)
Mg	n.d.	n.d.	n.d.	n.d.	0.13 (3)	0.03 (3)
Ti	n.d.	n.d.	n.d.	n.d.	0.02 (1)	0.01 (1)
□	0.00 (0)	0.00 (0)	0.00 (0)	0.17 (1)	0.00 (0)	0.00 (0)
Z site						
Al	5.97 (4)	5.96 (4)	5.92 (8)	6.00 (0)	6.00 (0)	6.00 (0)
Si	0.03 (4)	0.04 (4)	0.08 (8)	0.00 (0)	0.00 (0)	0.00 (0)
X site						
Na	0.84 (2)	0.66 (7)	0.57 (9)	0.58 (1)	0.57 (5)	0.41 (4)
Ca	n.d.	n.d.	n.d.	n.d.	0.21 (3)	0.28 (2)
K	n.d.	n.d.	n.d.	n.d.	0.01 (1)	0.00 (0)
□	0.16 (2)	0.34 (7)	0.43 (9)	0.42 (1)	0.22 (3)	0.31 (4)
V,W site						
O^{2-}	0.32 (22)	1.25 (9)	1.47 (9)	0.66 (4)	1.42 (27)	2.06 (10)
OH	3.68 (22)	2.75 (9)	2.53 (9)	3.34 (4)	2.58 (27)	1.94 (10)

n.d. = not determined; n = number of analyses; * Calculated from SREF and normalized to 100 wt%. Standard deviation = 1 σ

Table 2. Crystallographic data and refinement details for SREF of a synthetic columnar olenite with $^{[4]}$B

a, *c* (Å)	15.613(5), 7.043(2)
V (Å^3)	1486.8(8)
Crystal dimensions (mm)	60 x 25 x 25
Collection mode, $2\theta_{max}$ (°)	full sphere, 59.97
h, k, l ranges	-21/21, -21/21, -9/8
Total reflections measured	13131
Unique reflections	1032
$R1^*(F)$, $wR2^{\dagger}(F^2)$, $R_{int}^{\ddagger}$ (%)	1.94%, 4.10%, 4.26%
Flack *x* parameter	-0.04(14)
'Observed' refls. [$F_o > 4\sigma_{(Fo)}$]	1009
No. of refined parameters	95
Goodness-of-Fit§	1.113
$\Delta\sigma_{min}$, $\Delta\sigma_{max}$ (e/Å^3)	-0.43, 0.30

Notes: X-ray radiation: MoKα (λ = 0.71073 Å); *Z*: 3; space group: *R*3*m* (no. 160); multi-scan absorption correction; refinement on F^2. Frame width, scan time, detector distance: 2°, 250 s, 35 mm. Scan mode: sets of ϖ and θ scans.

* $R1 = \Sigma| |F_o| - |F_c| | / \Sigma|F_o|$
† $wR2 = \{\Sigma[w(F_o^2 - F_c^2)^2] / \Sigma[w(F_o^2)^2]\}^{1/2}$
$w = 1 / [\sigma^2(F_o^2) + (aP)^2 + bP]$, $P = [2F_c^2 + \mathrm{Max}(F_o^2,0)] / 3$
‡ $R_{int} = \Sigma|F_o^2 - F_o^2(\mathrm{mean})| / \Sigma[F_o^2]$
§ $\mathrm{GooF} = S = \{\Sigma[w(F_o^2 - F_c^2)^2] / (n-p)\}^{1/2}$

Table 3. Atom coordinates, isotropic (U_{iso}) or equivalent isotropic (U_{eq}) displacement parameters and site-occupancy factors (Occ.) from SREF of a synthetic columnar olenite with $^{[4]}B$

Site	x	y	z	U_{iso} /U_{eq} (Å^2)	Occ.
X	0	0	0.2246(6)	0.0297(14)	$Na_{0.58(1)}$
Y	0.12127(6)	1/2x	-0.33845(12)	0.0065(2)	$Al_{0.944(4)}$
Z	0.29700(4)	0.26155(4)	-0.37402(9)	0.00720(12)	$Al_{1.00}$
B	0.1090(1)	2x	0.4701(4)	0.0071(5)	$B_{1.00}$
T	0.18936(2)	0.18795(4)	0.02152(8)	0.00658(18)	$Si_{4.6}B_{1.4(1)}$
H3	0.247(3)	1/2x	0.438(6)	0.031(14)§	$H_{1.00}$
O1	0	0	-0.2134(5)	0.0075(6)	$O_{1.00}$
O2	0.05999(6)	2x	0.5132(3)	0.0076(4)	$O_{1.00}$
O3	0.25514(14)	1/2x	-0.4733(3)	0.0089(4)	$O_{1.00}$
O4	0.09471(7)	2x	0.0938(3)	0.0131(4)	$O_{1.00}$
O5	0.18699(14)	1/2x	0.1138(3)	0.0129(4)	$O_{1.00}$
O6	0.19221(8)	0.18216(8)	-0.20477(19)	0.0075(2)	$O_{1.00}$
O7	0.28498(8)	0.28468(8)	0.09167(18)	0.0079(2)	$O_{1.00}$
O8	0.20974(9)	0.27005(9)	0.45452(17)	0.0070(3)	$O_{1.00}$

for definition of U_{eq} see Fischer and Tillmanns (1988); § isotropic displacement parameter U_{iso}; Standard deviation = 1 σ

39

Table 4. Selected interatomic distances in synthetic columnar olenite with $^{[4]}$B from SREF

X-		*Y*-		*Z*-		*T*-		B-	
O2 x3	2.601(4)	O1	1.8611(17)	O6	1.8990(14)	O7	1.5808(13)	O2	1.360(3)
O5 x3	2.646(2)	O6 x2	1.9005(14)	O8	1.8633(13)	O6	1.5982(15)	O8 (x2)	1.367(2)
O4 x3	2.722(3)	O2 x2	1.9371(13)	O7	1.8808(14)	O4	1.5740(9)	Mean	1.365(2)
Mean	2.656(3)	O3	2.0440(21)	O8’	1.8743(14)	O5	1.5949(10)		
		Mean	1.930(1)	O7’	1.9100(13)	Mean	1.587(1)		
				O3	1.9811(12)				
				Mean	1.901(1)				

Standard deviation = 1 σ

Table 5a. Fitting parameters for the Raman spectra of the synthetic tourmaline (E || *c*)

Band	*Acicular crystal (core); n = 1* $^{[4]}B = 2.53\ (25)$			*Acicular crystal (rim); n = 4* $^{[4]}B = 1.43\ (15)$			*Columnar crystal; n = 4* $^{[4]}B = 1.18\ (15)$		
	Raman shift (cm^{-1})	FWHM (cm^{-1})	I_{rel} (%)	Raman shift (cm^{-1})	FWHM (cm^{-1})	I_{rel} (%)	Raman shift (cm^{-1})	FWHM (cm^{-1})	I_{rel} (%)
ν1	3301 (6)	165 (6)	15 (2)	3297 (16)	135 (14)	17 (5)	3284 (6)	103 (20)	16 (3)
ν2	3367 (1)	89 (2)	43 (2)	3368 (3)	88 (8)	34 (10)	3370 (4)	89 (4)	27 (4)
ν3	3458 (1)	52 (2)	16 (1)	3454 (1)	56 (5)	25 (11)	3451 (3)	56 (4)	42 (4)
ν4	3498 (1)	19 (2)	24 (1)	3498 (4)	50 (3)	21 (8)	3498 (5)	49 (5)	12 (3)
ν5	3556 (1)	21 (2)	0.3 (1)	3556 (4)	27 (3)	0.7 (3)	3554 (2)	27 (2)	0.8 (1)
ν6	3601 (1)	52 (2)	1.4 (1)	3603 (1)	51 (17)	3 (1)	3602 (1)	43 (14)	2.1 (8)

Table 5b. Fitting parameters of the Raman spectra of the natural Koralpe tourmaline (E || *c*)

Band	*Koralpe (core); n = 3* $^{[4]}B = 0.33\ (6)$			*Koralpe (rim); n = 3* $^{[4]}B = 0.67\ (12)$		
	Raman shift (cm^{-1})	FWHM (cm^{-1})	I_{rel} (%)	Raman shift (cm^{-1})	FWHM (cm^{-1})	I_{rel} (%)
ν1	not observed			not observed		
ν2	3385 (3)	143 (4)	14 (2)	3390 (5)	145 (3)	22 (2)
ν3	3471 (2)	66 (2)	47 (3)	3462 (1)	69 (1)	50 (2)
ν4	3522 (1)	50 (3)	17 (3)	3517 (1)	44 (1)	10 (1)
ν7	3562 (1)	39 (1)	13 (2)	3551 (1)	36 (1)	6 (1)
ν8	3601 (1)	30 (3)	6 (1)	3597 (1)	44 (1)	8.9 (2)
ν9	3641 (5)	34 (7)	1.7 (5)	3653 (1)	19 (1)	1.5 (1)
ν10	3666 (1)	9 (1)	0.7 (1)	3668 (1)	9 (1)	0.4 (1)
ν11	3675 (1)	9 (1)	0.7 (1)	3677 (1)	13 (1)	0.4 (1)
ν12	3682 (1)	23 (7)	0.3 (1)	3703 (1)	22 (1)	0.4 (1)

n = number of analyses. FWHM = full width at half maximum. I_{rel} = relative integrated intensity, *i.e.* peak area normalized to the total area. Standard deviation (1 σ) was calculated by averaging the results of n individual fits except for the spectrum of the acicular crystal core, where standard deviation (1 σ) is derived from the fit itself.

Table 6. Raman band assignment

Band	YZZ	YYY	O	T	X
ν1	AlAlAl		O3	Si-B	□
ν2	AlAlAl		O3	Si-B	Na
ν3	AlAlAl		O3	Si-Si	□
ν4	AlAlAl		O3	Si-Si	Na
ν5		AlAlAl	O1	Si-Si / Si-B	□
ν6		AlAlAl	O1	Si-Si / Si-B	Na
ν7	Fe^{2+}AlAl ?		O3	Si-Si	Na ?
ν8	LiAlAl ?		O3	Si-Si	Na ?
ν9		AlAlLi ?	O1	Si-Si / Si-B	Na ?
ν10		AlAlLi ?	O1	Si-Si / Si-B	Ca ?
ν11		AlAl□ ?	O1	Si-Si / Si-B	Na ?
ν12		AlAl□ ?	O1	Si-Si / Si-B	Ca ?

? = assignment ambiguous. For further explanation see text.

Figure 1

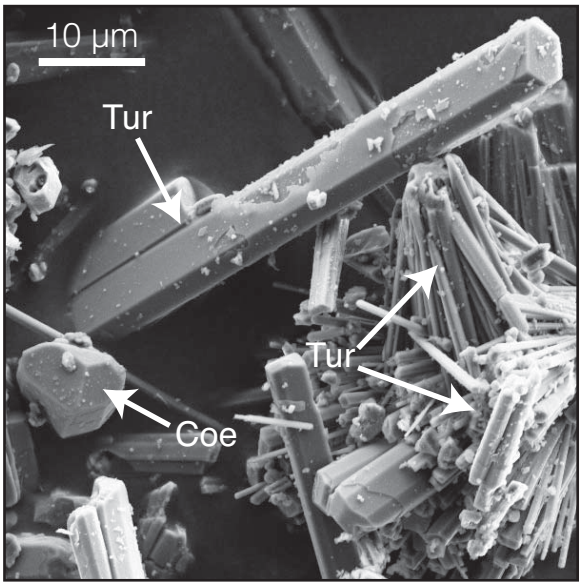

Figure 2

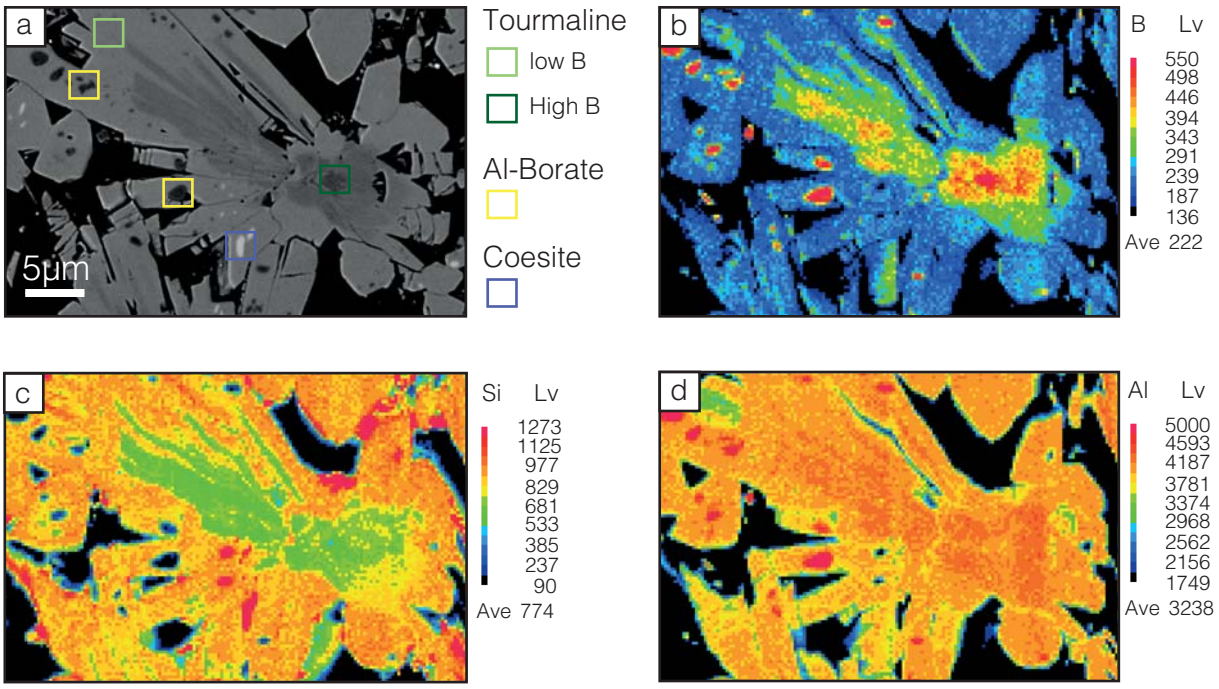
a
5μm
Tourmaline
low B
High B
Al-Borate
Coesite
b
B Lv
550
498
446
394
343
291
239
187
136
Ave 222
c
Si Lv
1273
1125
977
829
681
533
385
237
90
Ave 774
d
Al Lv
5000
4593
4187
3781
3374
2968
2562
2156
1749
Ave 3238

Figure 3

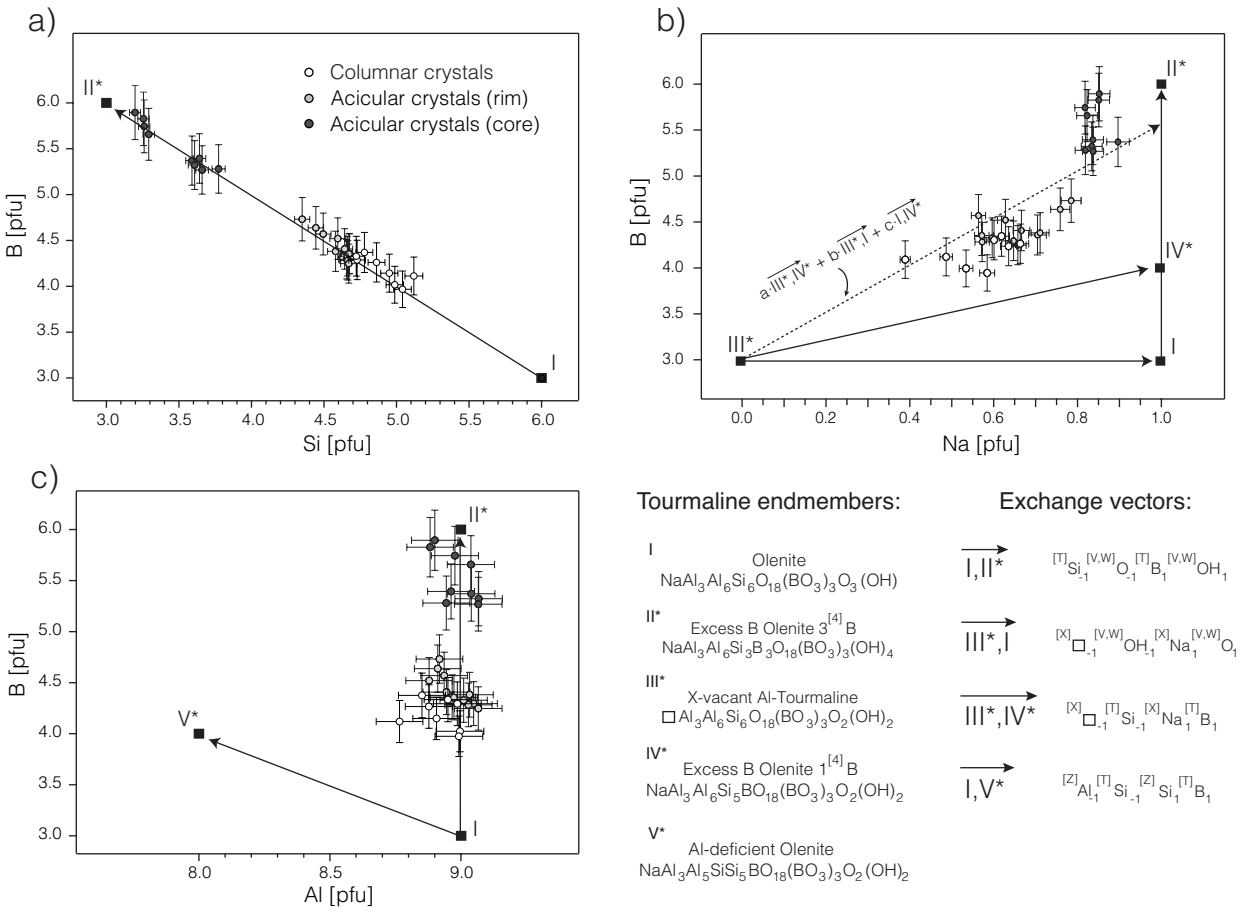
a)
Columnar crystals
Acicular crystals (rim)
Acicular crystals (core)
II*
I
B [pfu]
Si [pfu]
b)
II*
IV*
III*
I
a·III*,IV* + b·III*,I + c·I,IV*
B [pfu]
Na [pfu]
c)
II*
V*
I
B [pfu]
Al [pfu]
Tourmaline endmembers:
I
Olenite
NaAl3Al6Si6O18(BO3)3O3(OH)
II*
Excess B Olenite 3[4]B
NaAl3Al6Si3B3O18(BO3)3(OH)4
III*
X-vacant Al-Tourmaline
□Al3Al6Si6O18(BO3)3O2(OH)2
IV*
Excess B Olenite 1[4]B
NaAl3Al6Si5BO18(BO3)3O2(OH)2
V*
Al-deficient Olenite
NaAl3Al5SiSi5BO18(BO3)3O2(OH)2
Exchange vectors:
I,II*
[T]Si-1[V,W]O-1[T]B1[V,W]OH1
III*,I
[X]□-1[V,W]OH1[X]Na1[V,W]O1
III*,IV*
[X]□-1[T]Si-1[X]Na1[T]B1
I,V*
[Z]Al-1[T]Si-1[Z]Si1[T]B1

Figure 4

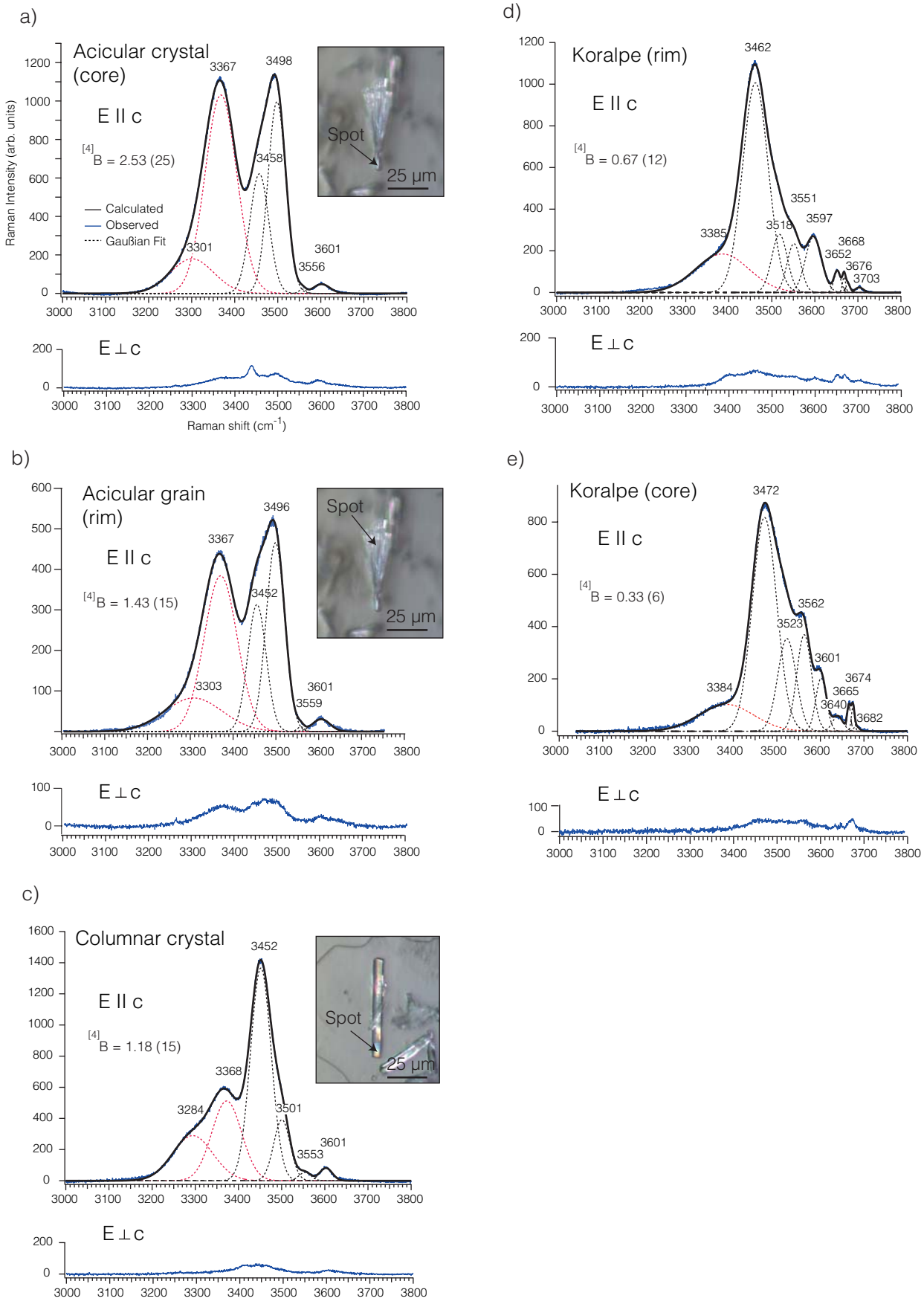
a)
Acicular crystal (core)
E II c
[4]B = 2.53 (25)
Calculated
Observed
Gaußian Fit
Raman Intensity (arb. units)
Raman shift (cm-1)
E ⊥ c
Spot
25 µm
b)
Acicular grain (rim)
E II c
[4]B = 1.43 (15)
c)
Columnar crystal
E II c
[4]B = 1.18 (15)
d)
Koralpe (rim)
E II c
[4]B = 0.67 (12)
e)
Koralpe (core)
E II c
[4]B = 0.33 (6)

Figure 5

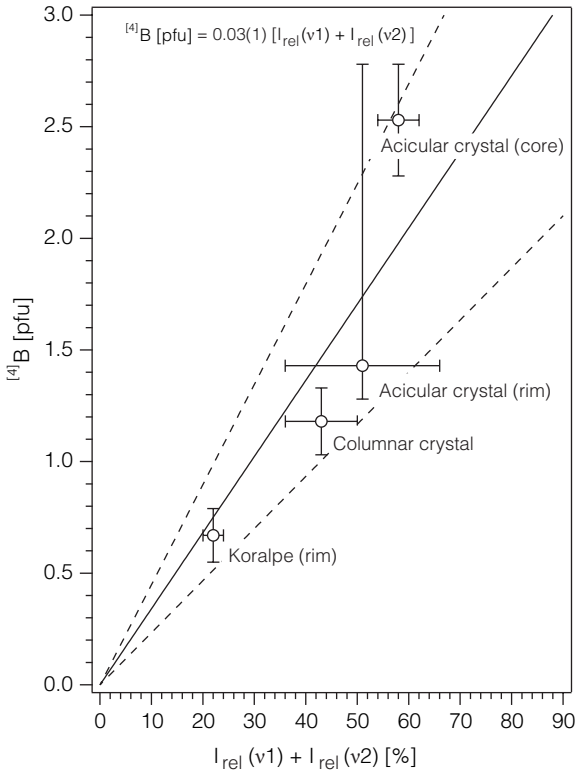
[4]B [pfu] = 0.03(1) [I rel (ν1) + I rel (ν2)]
Acicular crystal (core)
Acicular crystal (rim)
Columnar crystal
Koralpe (rim)
[4]B [pfu]
I rel (ν1) + I rel (ν2) [%]
0.0
0.5
1.0
1.5
2.0
2.5
3.0
0
10
20
30
40
50
60
70
80
90